Probing Two Distinct Types of Topological Rainbow Concentrators Related to the Acoustic Valley Hall Insulator in Synthesized Three-Dimensional Space

Zhennan Wang,[1] Zhenyu Wang,[2] Houyin Li,[1] Zhenzhen Liu,[1] Jinlong Luo,[1] Feijie Huang,[1] Jian Huang,[1] Xiaoyan Wang,[1] Hui Li,[1] and Hai Yang[1,*]

[1]*Key Laboratory of Artificial Microstructures in Yunnan Higher Education Institutions, School of Physics Science and Technology, Kunming University, Kunming 650214, China*

[2]*Key Laboratory of Artificial Micro- and Nanostructures of Ministry of Education and School of Physics and Technology, Wuhan University, Wuhan 430072, China*

Synthesized three-dimensional space provides us with a platform to explore the intriguing acoustic valley Hall insulator. In this paper, a rotational degree of freedom is introduced to construct a synthetic three-dimensional space. Based on simulations, our results show that Weyl points and Fermi arcs and topologically nontrivial edge modes appear in a synthetic space. Not only rotational operation but also boundary truncation can modulate the frequencies of nontrivial edge states, which result in two completely different edge states at the upper and lower boundaries. Using frequencies of edge states protected by Weyl points, we devise two different acoustic topological rainbow devices. The two devices are able to trap states with different frequency components at different spatial positions: one device is capable of capturing low-frequency components at close range, while the other has the ability to confine low-frequency components at long distances. This work may boost further the development of topological rainbow devices in a synthetic space related to the acoustic valley Hall insulator.

I. INTRODUCTION

Rainbow trapping, which refers to the fact that waves of different frequencies can be captured at different spatial positions [1–10], has attracted intense attention. Synthetic space—that is, the combination of physical dimensions with geometric dimensions to form higher-dimensional synthetic space—provides us with an avenue to explore topological phases and the higher than apparent geometrical dimensionality of samples [11–13]. Recently, Lu, Chan, and coworkers have implemented topological rainbow concentrators in an optical system based on synthetic dimensions [14,15]. The topological rainbow concentrator collects weak signals and captures light waves of different frequencies at different spatial locations.

Moreover, Weyl points (WPs) [16–22], possessing twofold-linear-degeneracy points in three-dimensional (3D) momentum space, have numerous special properties, such as chiral anomaly [23–25] and topological Fermi arc and edge states [21,22,26,27]. However, the exploration of Weyl physics in real 3D space is very troublesome. Lately, researchers have investigated the topological properties of

WPs in synthetic 3D parameter space, in which the synthetic space is constructed by introducing two additional structural parametric dimensions plus one physical dimension [28–31]. It is worth noting that synthetic WPs can induce topological edge states at the boundary between a photonic crystal and any reflection substrates [30] or between sonic crystals (SCs) [29,31] and a rigid wall. Then, a question naturally arises: can topological edge states induced by synthetic WPs be used to design the acoustic topological rainbow concentrator?

In this paper, we report two different topological rainbow concentrators based on exploring WPs in 3D synthetic space that is formed by two physical dimensions with the addition of a geometric dimension. As is known, in two-dimensional (2D) triangular-lattice SCs, there are degenerate points at K and K' in the first Brillouin zone [32–41] and the degeneracies are removed to form a complete band gap when the scatterers are rotated.

In this synthetic space, we observe synthetic WPs and synthetic Fermi arcs and the corresponding nontrivial edge states. In a certain angular range, we find that the frequencies of the nontrivial edge states increase monotonically with the increase of the rotational angle and thus we can construct an angular-gradient SC to realize a positive topological rainbow device, in which the edge states propagate further and further as the frequencies of the acoustic waves

*Corresponding author. kmyangh@263.net

decrease. In addition, we also design a negative topological rainbow device, designed by using a truncated SC, in which the frequencies of the topological edge states at the boundary between a truncated SC and the hard walls propagate over shorter and shorter distances as the frequencies of the edge states decrease in a certain boundary-truncation range. The robustness of the positive and negative topological rainbows is verified when the three main types of defects (cavities, disorder, and bending) are introduced at the boundaries.

Our work may open up a path for the realization of topological rainbow devices in acoustic systems and provide potential applications in concentrating weak signals and distributing different frequency components of topological states to different positions along the interface

of the SCs. Throughout our work, the simulations are performed using the commercial finite-element software COMSOL MULTIPHYSICS.

II. SYNTHESIZED WEYL POINTS AND THE CORRESPONDING NONTRIVIAL EDGE STATES

Figure 1(a) shows the designed SC, which is constructed by arranging a triangular-lattice array of three-legged rods in an air medium. For this system, the scatterers (blue regions) are regarded as the rigid body compared with the air background (gray region). In a unit cell, the lattice constant is $a = 2.0$ cm. Each scatterer is a three-legged rod and its length and width are $d = 0.7$ cm and $h = 0.2 \times \sqrt{3}$ cm, respectively. A rotational angle is denoted by the angle θ
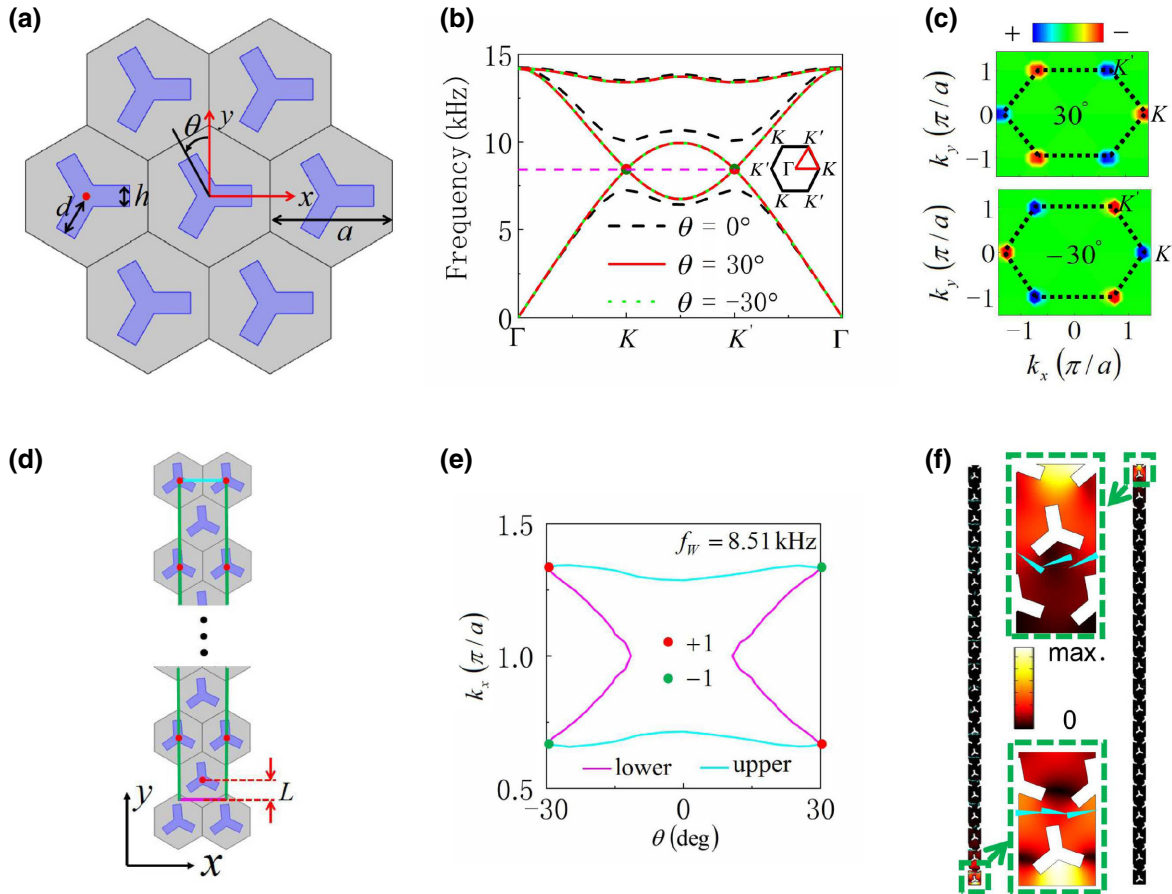

FIG. 1.   WPs synthesized by 2D triangular-lattice SCs. (a) A 2D triangular-lattice SC made of photosensitive resin (blue regions) immersed in an air background (gray region). (b) The dispersion relations of the SCs with $\theta = 0°$ (dashed black lines), $30°$ (solid red lines), and $-30°$ (dotted green lines). The solid red and green spheres represent WPs with different chiralities, which are marked as $+1$ and -1 in (e), respectively. (c) The Berry curvature of 2D SCs with $\theta = -30°$ and $30°$. (d) A ribbon-shaped supercell composed of 40 unit cells with $\theta = 10°$. (e) The equifrequency contours of the two pink (blue) Fermi arcs connecting to two Weyl points with distinct chiral charges in the vertical (horizontal) direction in the synthetic space (k_x, θ). The positive and negative WPs are labeled as $+1$ and -1, respectively. (f) The total-pressure-field distributions of two edge states with the same frequency (7.91 kHz) of the upper and lower boundaries in the case of $\theta = 10°$. The two insets in the middle show enlarged views of the upper and lower boundaries and the red arrows represent the energy flux of the acoustic waves.

relative to the y axis and the rotational center is the center of the unit cell (red point). The clockwise (counterclockwise) rotation of the scatterer is defined as $\theta < 0$ ($\theta > 0$). We choose the mass density and the wave velocity of air as 1.21 kg/m^3 and 343 m/s, respectively.

We display the dispersions of the SCs when $\theta = 0°$ and $\pm 30°$, as shown in Fig. 1(b). The solid red and green spheres represent WPs with different chiralities, which are marked as $+1$ and -1. The inset shows the first Brillouin zone. The horizontal dashed red line indicates the frequency of the four Weyl points with the same frequency (8.51 kHz) in Fig. 1(b). As is known, our 2D system belongs to the valley SCs [32–41], which must lead to two degeneracy points at the high-symmetry points K and K' due to the C_{3v} symmetry, and reduction of the symmetry forms a complete gap. Even though a pair of linear-degeneracy points occur at the high-symmetry points K and K', we only need consider one of the high-symmetry points owing to the time-reversal symmetry.

Sketches of the Berry curvature of the 2D SCs with $\theta = -30°$ and $30°$ are shown in Fig. 1(c). We detail the corresponding process of calculating the Berry curvature in Sec. A of the Supplemental Material [42,43]. The projection of the Berry curvature along the ΓK direction is used to judge the topological charge of the WPs. The rotational angle θ is able to change the dispersion relations of the triangular-lattice SCs, which can be regarded as a additional degree of freedom. In our 2D SCs, combining the 2D Bloch-wave vectors k_x, k_y and the extra structural parameter θ, we construct a synthetic 3D parameter space (k_x, k_y, θ), in which Weyl physics can be studied [26–29]. Dispersions of the first two bands and the edge states at the upper and lower boundaries in the synthetic space (θ, k_x) and the distribution of the WPs in synthetic space (k_x, k_y, θ) are provided in Sec. B of the Supplemental Material [42].

On the basis of previous work [29–31], we know that the synthetic WPs always accompany the topological edge states at the boundary between a truncated SC and a hard wall. To study the topological properties of the edge states, we design a supercell with a specific boundary truncation, including 40 unit cells with $\theta = 10°$, as depicted in Fig. 1(d). We choose the cyan line between the centers of two adjacent unit cells as the upper boundary, regard the connection of two centers of the side lengths of the adjacent hexagons (pink line) as the lower boundary, and then consider the position $L = 0.5\sqrt{3}$ cm as the starting position of the lower boundary truncation. The solid cyan and pink horizonal lines mark the upper and lower boundaries, respectively, the two solid green vertical lines correspond to the left and right boundaries, and then the two horizonal lines and two vertical lines form a rectangle. The hard boundary conditions are imposed on the upper and lower boundaries and the periodic boundary conditions are implied on the left and right boundaries.

By varying the rotational angle θ, we show the equifrequency contours of the four WPs in the synthetic parameter space (k_x, θ), as shown in Fig. 1(e). It is notable that the two pink (cyan) Fermi arcs at the lower (upper) boundary connect to the two WPs with distinct chiral charges in the vertical (horizontal) direction. The four WPs share the same frequency of 8.51 kHz. The rotational-angle dependence of the dispersions of the upper and lower edge states at $k_x = 2\pi/3a$ are shown in Sec. C of the Supplemental Material [42].

Meanwhile, the corresponding total-pressure-field distributions are depicted in Fig. 1(f). Through inspecting the corresponding distributions, we observe that the topological edge states include the lower edge states (pink surface, positive group velocity) at the lower boundary and the upper edge states (cyan surface, negative group velocity) at the upper boundary (as shown in Sec. B of the Supplemental Material [42]) and these edge states are tightly confined around the lower or upper boundaries. We also demonstrate the robustness of the edge states at the lower boundary by introducing three types of defects, i.e., cavities, disorder, and bending, in Sec. D of the Supplemental Material [42].

III. TWO DISTINCT TOPOLOGICAL RAINBOW CONCENTRATORS

We now focus mainly on the frequency shifts of the topological edge states at the lower boundary, which can be used to design a topological rainbow concentrator. In general, the dispersion relations are symmetric with respect to the line $k_x = 0$ and thus we only study the left half or right half of the dispersion relations, as long as the corresponding group velocities are in agreement with the directions of the incident sounds.

As shown in Fig. 2(a), we design a graded SC, in which the rotational angles present the monotonic decreases from 25° (the first column, on the far left) to 10° (the 31st column, on the far right) along the θ axis. For this gradient SC, the rotational angles decrease when the column numbers increase gradually and the starting and ending angles are $\theta_1 = 25°$ and $\theta_{31} = 10°$, respectively. The rotational interval $\Delta\theta = (\theta_{31} - \theta_1)/(31 - 1) = -0.5°$. Hence the rotational angle $\theta(n)$ in the nth column can be denoted as $\theta(n) = \Delta\theta(n - 1) + \theta_1$.

Changing the rotational angle, we find that the edge states have monotonic changes. Avoiding the edge states that are too close to be distinguished in the dispersion relation of the edge states at the lower boundary, we show an enlargement of the dispersion relation within $[0.8, 1]$ (π/a), as shown in Fig. 2(b). The inset is the dispersion relation within $[0, 1]$ (π/a). The horizontal dashed pink lines indicate the frequency of the four WPs in Figs. 2(b) and 2(c). We choose seven rotational angles to display the frequency shifts. At $k_x = \pi/a$, we observe that
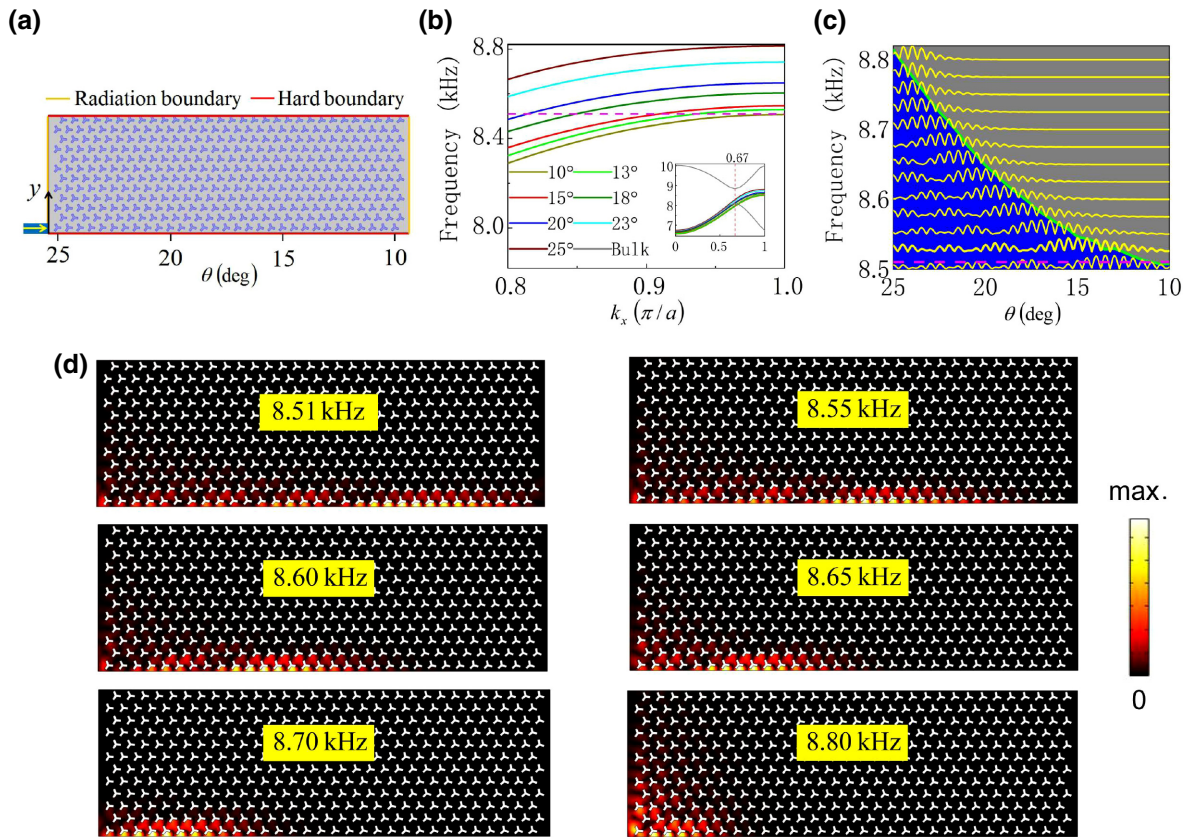
FIG. 2. A topological rainbow concentrator based on rotation. (a) A schematic diagram of the topological rainbow concentrator, consisting of gradient SCs. The solid yellow lines represent the radiation boundary conditions. The yellow arrow and the blue rectangle at the far left of the concentrator show the direction and width of the Gaussian beam, respectively. (b) The dispersion relations of the edge states at the lower boundary. (c) The normalized intensity distributions along the lower boundary in (a). The blue and gray parts are the regions of existence and nonexistence of the edge states, respectively. (d) The total-pressure-field distributions of the edge states corresponding to different frequencies.

the frequencies of the lower edge states increase monotonically as the rotational angles increase. Here, the rotational angles θ are chosen as $10°$, $13°$, $15°$, $18°$, $20°$, $23°$, and $25°$, respectively. The frequencies of the four Weyl points (8.51 kHz) at the lower boundary, at $k_x = \pi/a$, are located at the lower-frequency limit of the edge states and very close to the bulk band. It is worth noting that the bulk bands also change in this process. This property of the lower edge states in the bulk gap plays a key role in devising the topological rainbow concentrators. Most of the frequencies of the topological rainbows are related to the acoustic valley Hall insulator and the acoustic valley Chern numbers of this system are given in Sec. E of the Supplemental Material [39,42,44–46].

In Fig. 2(c), we show the normalized intensity distributions along the lower boundary within a certain frequency range. The results demonstrate that the acoustic waves of different frequencies stop at different positions, as predicted by the solid yellow curves. It is where the edge states stop propagating that the amplitudes of the

edge states reach their maximum, as shown in Fig. 2(c). The total-pressure-field distributions around the lower boundaries are shown in Fig. 2(d), where the six frequencies are selected to show the topological rainbow. Figure 2(d) shows that the frequencies of the edge states increase and the propagation distances along the lower boundary become shorter and shorter with the increase in frequency. We note that the distributions of the acoustic pressure field of the edge states in the vertical direction become narrower and narrower when acoustic waves propagate through the sample, which indicates that the localization is more intensive.

Our next objective is to design different rainbow devices based on the frequency shift of the topological edge states at the upper boundary, modulated by the boundary truncation. In Fig. 3(a), we design the other gradient SC, in which the boundary truncations display monotonic increases from 0 (the first column, on the far left) to $0.3\sqrt{3}$ cm (the 31st column, on the far right) along the number axis n. In fact, the whole rectangle in Fig. 1(d)
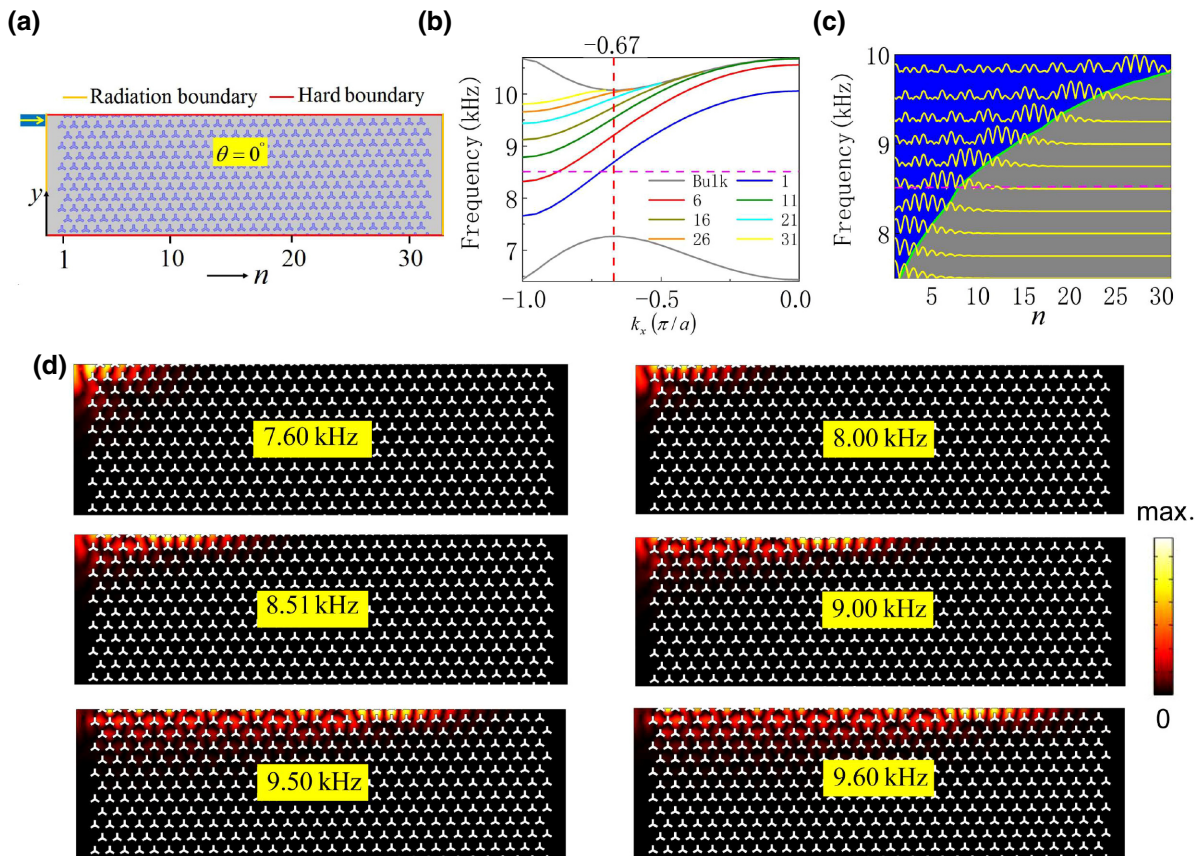
FIG. 3. A topological rainbow concentrator based on boundary truncation. (a) A schematic diagram of the topological rainbow concentrator, which is a gradual SC (the boundary truncation of the scatterers in each column is larger by $0.01\sqrt{3}$ cm than those in the previous column). (b) The dispersion relations of the edge states at the upper boundary. The column numbers n are 1, 6, 11, 16, 21, 26, and 31, respectively. The rotational angles are chosen as $0°$: in this case, the concentrator has a maximum width of the bulk gap. (c) The normalized intensity distributions along the upper boundary in (a). The blue and gray parts are the regions of existence and nonexistence of the edge states, respectively. (d) The total-pressure-field distributions of the edge states corresponding to different frequencies.

moves downward and then the upper boundary (horizontal cyan line) and lower boundary (horizontal pink line) simultaneously shift downward.

Here, we construct a gradient SC with $\theta = 0°$. The biggest bulk gap appears under these circumstances. The value of L, which depicts the boundary truncation, becomes larger when the column numbers increase gradually. The positions of L and L_1 overlap and the starting and termination points of the upper boundaries are at $L_1 = 0$ cm and $L_{31} = 0.3\sqrt{3}$ cm, respectively. The interval of the boundaries between the two closest columns $\Delta L = (L_{31} - L_1)/(31 - 1) = 0.01\sqrt{3}$ cm. Then, the L_n of the nth column can be written as $L_n = 0.5\sqrt{3} + \Delta L(n - 1)$, where L_n refers to the distance of the downward movement for the lower boundary.

In Fig. 3(b), we find that the frequencies of the upper edge states (the left-half part of the dispersion relations) shift upward gradually with increasing n (L_n). We

choose seven frequencies corresponding to seven truncated boundaries, in order to show the frequency shifts. At $k_x = -\pi/a$, we observe that the frequencies of the edge states at the upper boundaries increase monotonically as the column numbers increase and in the meantime the bulk bands remain unchanged. This property plays a role in designing the topological rainbow concentrator. The WPs of the upper boundary emerge in the middle of the frequency region of the edge states and the horizontal dashed red line indicates the frequency (8.51 kHz) of the WPs of the lower boundary, as shown in Figs. 3(b) and 3(c).

The normalized intensity distributions of the upper edge states, along the upper boundaries, are shown in Fig. 3(c). The results are quite the opposite of those in Fig. 2(c). The acoustic waves of the higher frequencies propagate further than those of the lower frequencies. It is where the edge states cease to propagate that the amplitudes of the edge states reach their maximum, as shown in Fig. 3(c). The

total-pressure-field distributions around the upper boundaries are shown in Fig. 3(d) and six frequencies are selected to show the topological rainbow concentrator. When the frequencies increase, the acoustic waves propagate further and further away. Additionally, we present the case of the upper (lower) edge states modulated by the rotational angle (the boundary truncation) in Sec. F of the Supplemental Material [42]. However, in those cases, the edge states do not show the monotonic properties and thus cannot be used to design the rainbow effect.

To experimentally detect the two completely different topological rainbow effects, we measure the transmission intensity at the boundaries for the two gradient SCs. In the experiment, the three-legged rods in the SC are precisely fabricated via 3D printing and are composed of epoxy resin. The height of the rods, which are placed between the cover plate (Plexiglas) and the bottom plate (epoxy resin), is chosen to be 1.3 cm. In this scenario, the two-dimensional approximation is applicable. Our experimental setup is immersed in an air background. Acoustic foam is mounted around the surroundings of the SCs to minimize the boundary reflections due to the open space.

We measure the sound-transmission intensity along the specific boundaries for the positive and negative topological rainbow concentrators discussed above. First, we measure the transmission intensity along the lower boundary of the SC with the gradient distributions of the rotational angles, as shown in Fig. 4(a). Next, we also measure the transmission intensity along the upper boundary of the SC with the gradient distributions of the boundary truncation. The distributions of the normalized intensity spectra along the upper boundary for the different frequencies and boundary truncations are depicted in Fig. 4(b). Acoustic waves with frequency 7.5 kHz can be captured at the position of $n = 1$, with the shortest distance of propagation. As the column numbers increase, the propagation distances

become longer and longer. The experimental data reproduce the numerical results excellently. Comparing Fig. 2(c) to Fig. 3(c), these two completely different rainbow effects are caused by the rotation operation and boundary truncation. In short, the two devices can concentrate weak signals and distribute different frequency components of topological edge states to different locations along the boundaries, enabling frequency routing in real space.

We observe that the distributions of the normalized intensity spectra of the edge states along the lower boundary are wider than those along the upper boundary. The distinctive behavior of the edge states in the dispersion relations causes this situation to occur. Comparing Figs. 2(b) and 3(b), we note that the slopes ($d\omega/dk_x$) of the edge states at the lower boundary are always positive in Fig. 2(b) but those at the upper boundary in Fig. 3(b) are negative at all times. When wave vector k_x is smaller than $0.67(\pi/a)$ in Fig. 2(b), almost all of the edge states at the lower boundary are within the bulk band. The group velocities (slopes) of the edge states of the maximum frequency first tend to almost zero when wave vector k_x approaches the right boundary of the first Brillouin zone. However, when k_x is within $[-1, -0.67](\pi/a)$ in Fig. 3(b), all of the edge states are in the band gap and the group velocities of the edge state of the minimum frequency first tend to almost zero when k_x approaches the left boundary of the first Brillouin zone. It is clear that where the acoustic waves stop spreading is in which the amplitudes of the edge states reach maximum values, as shown in Figs. 2(c) and 3(c). The band gap (2.80 kHz) in Fig. 3(b) is wider than that (0.76 kHz) in Fig. 2(b) and is 3.68 times that shown in Fig. 2(b). The edge states in Fig. 3(b) are more widely distributed than those in Fig. 2(b) in 1D reciprocal space. Consequently, from 1D reciprocal space into 1D real space, the distributions of the edge states at the lower boundary in Fig. 2(b) are wider than those at the upper boundary in Fig. 3(b). On the basis of our simulation test, we also demonstrate the robustness of the two distinct topological rainbow concentrators by introducing some perturbations at the boundaries in Sec. G of the Supplemental Material [42].

IV. CONCLUSIONS

In summary, synthesized WPs are realized in synthetic 3D space, which leads to the existence of topological edge states at the upper and lower boundaries. By modulating the rotation and the boundary truncation, the frequencies of the edge states can be shifted monotonically. On the basis of the rotation and boundary truncation, we can design two completely different types of topological rainbow devices related to the WPs. These results are demonstrated in simulations and experiments. This work may provide a platform for exploring acoustic topological rainbow devices connected to WPs in synthetic parameter space.
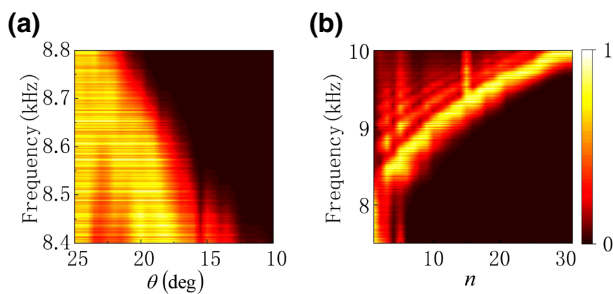

FIG. 4. The experimental observation of the completely different topological rainbow concentrators. (a) The normalized intensity distributions along the lower boundary. The light and dark parts are the regions of existence and nonexistence of the edge states, respectively. (b) The normalized intensity distributions along the upper boundary.

ACKNOWLEDGMENTS

———————

[1] K. L. Tsakmakidis, A. D. Boardman, and O. Hess, ′Trapped rainbow′ storage of light in metamaterials, Nature (London) **450,** 397 (2007).

[2] H. Kurt and H. D. Yilmaz, Rainbow trapping using chirped all-dielectric periodic structures, Appl. Phys. B **110,** 411 (2013).

[3] H. Jia, M. Lu, X. Ni, M. Bao, and X. Li, Spatial separation of spoof surface acoustic waves on the groove grating, J. Appl. Phys. **116,** 124504 (2014).

[4] G. J. Chaplain, D. Pajer, J. M. D. Ponti, and R. V. Craster, Delineating rainbow reflection and trapping with applications for energy harvesting, New J. Phys. **22,** 063024 (2020).

[5] Q. Gan, Y. J. Ding, and F. J. Bartoli, Rainbow Trapping and Releasing at Telecommunication Wavelengths, Phys. Rev. Lett. **102,** 056801 (2009).

[6] Z. Tian, C. Shen, J. Li, E. Reit, H. Bachman, J. E. S. Socolar, S. A. Cummer, and T. J. Huang, Dispersion tuning and route reconfiguration of acoustic waves in valley topological phononic crystals, Nat. Commun. **11,** 762 (2020).

[7] G. J. Chaplain, J. M. D. Ponti, G. Aguzzi, A. Colombi, and R. V. Craster, Topological Rainbow Trapping for Elastic Energy Harvesting in Graded Su-Schrieffer-Heeger Systems, Phys. Rev. Appl. **14,** 054035 (2020).

[8] B. Ungureanu, M. P. Makwana, R. V. Craster, and S. Guenneau, Localizing Elastic Edge Waves via the Topological Rainbow Effect, Phys. Rev. Appl. **15,** 014057 (2021).

[9] H. Wu, Y. Yin, Z. Sheng, Y. Li, D. Qi, and R. Peng, Multi-band Omnidirectional Ventilated Acoustic Barriers Based on Localized Acoustic Rainbow Trapping, Phys. Rev. Appl. **15,** 054033 (2021).

[10] J. M. De Ponti, L. Iorio, E. Riva, R. Ardito, F. Braghin, and A. Corigliano, Selective Mode Conversion and Rainbow Trapping via Graded Elastic Waveguides, Phys. Rev. Appl. **16,** 034028 (2021).

[11] L. Yuan, Q. Lin, M. Xiao, and S. Fan, Synthetic dimension in photonics, Optica **5,** 1396 (2018).

[12] M. Kim, Z. Jacob, and J. Rho, Recent advances in 2D, 3D and higher-order topological photonics, Light-Sci. Appl. **9,** 130 (2020).

[13] S. Ma, Y. Bi, Q. Guo, B. Yang, O. You, J. Feng, H. Sun, and S. Zhang, Linked Weyl surfaces and Weyl arcs in photonic metamaterials, Science **373,** 572 (2021).

[14] H. Zhang, L. Qian, C. Wang, C. Ji, Y. Liu, J. Chen, and C. Lu, Topological rainbow based on graded topological photonic crystals, Opt. Lett. **46,** 1237 (2021).

[15] C. Lu, C. Wang, M. Xiao, Z. Zhang, and C. Chan, Topological Rainbow Concentrator Based on Synthetic Dimension, Phys. Rev. Lett. **126,** 113902 (2021).

[16] M. Xiao, W. Chen, W. He, and C. Chan, Synthetic gauge flux and Weyl points in acoustic systems, Nat. Phys. **11,** 920 (2015).

[17] W. Chen, M. Xiao, and C. Chan, Photonic crystals possessing multiple Weyl points and the experimental observation of robust surface states, Nat. Commun. **7,** 13038 (2016).

[18] H. He, C. Qiu, X. Cai, M. Xiao, M. Ke, F. Zhang, and Z. Liu, Observation of quadratic Weyl points and double-helicoid arcs, Nat. Commun. **11,** 1820 (2020).

[19] M. Xiao, L. Ye, C. Qiu, H. He, Z. Liu, and S. Fan, Experimental demonstration of acoustic semimetal with topologically charged nodal surface, Sci. Adv. **6,** eaav2360 (2020).

[20] X. Huang, W. Deng, F. Li, J. Lu, and Z. Liu, Ideal Type-II Weyl Phase and Topological Transition in Phononic Crystals, Phys. Rev. Lett. **124,** 206802 (2020).

[21] H. He, C. Qiu, L. Ye, X. Cai, X. Fan, M. Ke, F. Zhang, and Z. Liu, Topological negative refraction of surface acoustic waves in a Weyl phononic crystal, Nature (London) **560,** 61 (2018).

[22] F. Li, X. Huang, J. Lu, J. Ma, and Z. Liu, Weyl points and Fermi arcs in a chiral phononic crystal, Nat. Phys. **14,** 30 (2018).

[23] A. A. Burkov and L. Balents, Weyl Semimetal in a Topological Insulator Multilayer, Phys. Rev. Lett. **107,** 127205 (2011).

[24] G. Xu, H. Weng, Z. Wang, X. Dai, and Z. Fang, Chern Semimetal and Quantized Anomalous Hall Effect in HgCr$_2$Se$_4$, Phys. Rev. Lett. **107,** 186806 (2011).

[25] X. Huang *et al.*, Observation of the chiral-anomaly-induced negative magnetoresistance in 3D Weyl semimetal TaAs, Phys. Rev. X **5,** 031023 (2015).

[26] S. Xu *et al.*, Discovery of a Weyl Fermion semimetal and topological Fermi arcs, Science **349,** 613 (2015).

[27] L. Lu, Z. Wang, D. Ye, L. Ran, L. Fu, J. D. Joannopoulos, and M. Soljacic, Experimental observation of Weyl points, Science **349,** 622 (2015).

[28] F. Zangeneh-Nejad and R. Fleury, Experimental observation of the acoustic Z_2 Weyl semimetallic phase in synthetic dimensions, Phys. Rev. B **102,** 064309 (2020).

[29] X. Fan, C. Qiu, Y. Shen, H. He, M. Xiao, M. Ke, and Z. Liu, Probing Weyl Physics with One-Dimensional Sonic Crystals, Phys. Rev. Lett. **122,** 136802 (2019).

[30] Q. Wang, M. Xiao, H. Liu, S. Zhu, and C. Chan, Optical interface states protected by synthetic Weyl points, Phys. Rev. X **7,** 031032 (2017).

[31] Z. Wang, Z. Wang, H. Li, J. Luo, X. Wang, Z. Liu, and H. Yang, Weyl points and nodal lines in acoustic synthetic parameter space, Appl. Phys. Express **14,** 077002 (2021).

[32] J. Lu, C. Qiu, M. Ke, and Z. Liu, Valley Vortex States in Sonic Crystals, Phys. Rev. Lett. **116,** 093901 (2016).

[33] J. Lu, C. Qiu, W. Deng, X. Huang, F. Li, F. Zhang, S. Chen, and Z. Liu, Valley Topological Phases in Bilayer Sonic Crystals, Phys. Rev. Lett. **120,** 116802 (2018).

[34] M. Wang, L. Ye, J. Christensen, and Z. Liu, Valley Physics in Non-Hermitian Artificial Acoustic Boron Nitride, Phys. Rev. Lett. **120,** 246601 (2018).

[35] Z. Zhang, Y. Tian, Y. Wang, S. Gao, Y. Cheng, X. Liu, and J. Christensen, Directional acoustic antennas based on valley-Hall topological insulators, Adv. Mater. **30,** 1803229 (2018).

[36] M. Yan, J. Lu, F. Li, W. Deng, X. Huang, J. Ma, and Z. Liu, On-chip valley topological materials for elastic wave manipulation, Nat. Mater. **17,** 993 (2018).

[37] Y. Shen, C. Qiu, X. Cai, L. Ye, J. Lu, M. Ke, and Z. Liu, Valley-projected edge modes observed in underwater sonic crystals, Appl. Phys. Lett. **114,** 023501 (2019).

[38] X. Han, Y.-G. Peng, L. Li, Y. Hu, C. Mei, D.-G. Zhao, X.-F. Zhu, and X. Wang, Experimental Demonstration of Acoustic Valley Hall Topological Insulators with the Robust Selection of C_3v-Symmetric Scatterers, Phys. Rev. Appl. **12,** 014046 (2019).

[39] Z. Zhu, X. Huang, J. Lu, M. Yan, F. Li, W. Deng, and Z. Liu, Negative Refraction and Partition in Acoustic Valley Materials of a Square Lattice, Phys. Rev. Appl. **12,** 024007 (2019).

[40] M. Wang, W. Zhou, L. Bi, C. Qiu, M. Ke, and Z. Liu, Valley-locked waveguide transport in acoustic heterostructures, Nat. Commun. **11,** 3000 (2020).

[41] Z. Wang, Y. Yang, H. Li, H. Jia, J. Luo, J. Huang, Z. Wang, B. Jiang, N. Yang, G. Jin, and H. Yang, Multichannel Topological Transport in an Acoustic Valley Hall Insulator, Phys. Rev. Appl. **15,** 024019 (2021).

[42] See the Supplemental Material at http://link.aps.org/supplemental/10.1103/PhysRevApplied.17.064002 for the Berry curvature of the first band, the dispersions of the first two bands and the edge states at the upper and lower boundaries in synthetic space (θ, k_x), the distributions of the WPs in synthetic space (k_x, k_y, θ), the rotational-angle dependence of the dispersion relations of the edge states at $k_x=2\pi/3a$, the robustness of the edge states at the lower boundary, the acoustic valley Chern numbers of this system, the edge states at the lower and upper boundaries modulated by boundary truncation and the rotational angle, respectively, and the robustness of the two distinct topological rainbow concentrators.

[43] C. Wang, H. Zhang, H. Yuan, J. Zhong, and C. Lu, Universal numerical calculation method for the Berry curvature and Chern numbers of typical topological photonic crystals, Front. Optoelectron. **13,** 73 (2020).

[44] J. Lu, C. Qiu, L. Ye, X. Fan, M. Ke, F. Zhang, and Z. Liu, Observation of topological valley transport of sound in sonic crystals, Nat. Phys. **13,** 369 (2017).

[45] H. Dai, T. Chen, J. Jiao, B. Xia, and D. Yu, Topological valley vortex manipulation of microparticles in phononic crystals, J. Appl. Phys. **126,** 145101 (2019).

[46] Z. Geng, Y. Peng, P. Li, Y. Shen, D. Zhao, and X. Zhu, Mirror-symmetry induced topological valley transport along programmable boundaries in a hexagonal sonic crystal, J. Phys.: Condens. Matter **31,** 245403 (2019).